Facile and scalable pulsed electrodeposition of bi-active Bi-Sb Alloy for high performance sodium ion batteries

Miaogen Chen [a,b], Xinyue Han [a,b], Xiaomei Zheng [a*], Hairui Shen [a], Jingkai Wang [a], Jinhai You [c], Lijing Yan [a], Xianhe Meng [a], Qiaoling Kang [a], Qiong Wu [a], Yue Zhao[a], Tingli Ma [a]

A *Magnetism Key Laboratory of Zhejiang Province, College of Materials and Chemistry, China Jiliang University, Hangzhou, 310018, China*

B *Key Laboratory of Intelligent Manufacturing Quality Big Data Tracing and Analysis of Zhejiang Province, College of Science, China Jiliang University, Hangzhou, 310018, China*

C *Laboratory for Soft Matter and Biophysics, Department of Physics and Astronomy, KU Leuven, Leuven 3001, Belgium*

*Corresponding authors:

E-mail: Zheng_xiaomei@cjlu.edu.cn

Abstract:

Although sodium ion batteries (SIB) have shown great potential for large-scale energy storage systems, the development of high-performance anode materials for SIB is crucial for their progress. However, the cycling performance of SIB is currently limited by severe volume changes during the sodiation/desodiation process. To overcome this problem, a bi-active metal alloying strategy has been proposed. In this study, we utilized pulsed electrodeposition to prepare bismuth-antimony alloy anode materials. The resulting $Bi_{44.9}Sb_{55.1}$ alloy anode exhibited exceptional specific capacity, rate performance, and stability. After the second cycle, the discharge/charge capacities were 505.3 $mAh \cdot g^{-1}$/496.7 $mAh \cdot g^{-1}$ at 1 $A \cdot g^{-1}$, with a coulombic efficiency of over 98%. Even after 50 cycles, the capacities remained at 494.7 $mAh \cdot g^{-1}$/481.9 $mAh \cdot g^{-1}$ with a capacity retention rate of 97.9%. These excellent properties were attributed to the stable structure and suitable voids for electron transport and ion diffusion in the $Bi_{44.9}Sb_{55.1}$ alloy, which effectively mitigated volume expansion during cycling. The reaction kinetics and mechanism were studied using cyclic voltammetry, in situ X-ray

diffraction, and nuclear magnetic resonance techniques. Our work provides valuable insights for the development of bi-active metal alloy anodes for SIB.

Keywords: Bi-Sb alloy, pulsed electrodeposition, in situ X-ray diffraction, nuclear magnetic resonance techniques, sodium ion battery

1. Introduction

With the rapid development of new energy vehicles and other innovations, the market demand for energy storage devices is increasing [1–4]. Traditional energy sources bring serious environmental problems, while sustainable energy sources are costly [5–8]. Lithium-ion batteries have become a strong contender for new energy for their high energy density and long cycling performance. However, the expensive price of lithium and the imbalanced geographical distribution of lithium resources limit its development [9,10]. In contrast, sodium-ion batteries (SIBs) become a strong competitor to replace lithium-ion batteries due to the low price of sodium and the abundance of resources [11]. Compared with the current development of cathode for SIBs, the advancement of its anode was slow [12]. In the studies that have been completed, the antimony-based anode shows moderate sodium storage performance [13,14]. In spite of this, it is still necessary to explore the anode materials equipped with excellent performance, and to investigate the mechanism of sodium storage for SIBs [15–17].

In recent years, significant research efforts have been dedicated towards developing promising metal anode materials, such as Sb, Bi, Sn, Zn, etc., due to their impressive theoretical capacities. Nonetheless, the use of metal anodes in cycling can result in significant volume expansion, which can cause capacity loss due to active material pulverization and shedding [17–19]. Fortunately, the issue mentioned above can be effectively addressed by using e.g., bi-active metal alloy, in which the two metals can provide a mechanical buffer for each other to mitigate volume expansion and also enhance conductivity [20]. Among the alloys studied, the bismuth-antimony (Bi-Sb) alloy stands out due to several advantages. Firstly, antimony is abundant and low-cost, making it an advantageous material. Additionally, the sodiation potential of antimony (~ 0.6 V vs. Na/Na^+) is suitable, ensuring the power density without inducing sodium dendrites at low voltage [21–23]. Meanwhile, Sb has a high theoretical capacity (660 $mAh \cdot g^{-1}$) and excellent electrical conductivity (2.4×10^6 $S \cdot m^{-1}$). However, desodiation/sodiation process of Sb anode can lead to significant volume expansion (390%), resulting in cracks and eventually structural fracture [24–26]. To address the aforementioned issue, an alternative approach to improve the electrochemical performance of SIBs is to utilize Bi-active metal alloys. Particularly, due to its distinctive layered structure, Bi boasts excellent ionic and electrical conductivity, and displays a favorable sodium voltage (~0.55 V vs. Na/Na^+), indicating its enormous

potential [27,28]. Additionally, Bi has a theoretical capacity of 385 mAh·g^{-1}, making it a promising candidate for use in improving the electrochemical performance of SIBs [29,30].

Various approaches have been attempted to prepared bi-active Bi-Sb anodes such as electrodeposition method, high energy ball milling method and hydrothermal method. Zhang et al. demonstrated the one-step production of nanosized $Bi_{0.70}Sb_{0.30}$ in ambient conditions using MOF as a precursor and laser as an energy source which showed a specific capacity of 259.8 mAh·g^{-1} at 0.2 A·g^{-1} after 500 cycles [31]. Gao et al. prepared nanoporous Bi-Sb alloys with different content ratios which were melted in a graphite crucible using an electric resistance furnace under the protection of covering flux, and then cast into a mold. The np-Bi_2Sb_6 electrode delivered a reversible capacity of 257.5 mAh·g^{-1} at 0.2 A·g^{-1} after 2000 cycles [32]. Compared to the above methods, pulsed electrodeposition method has various advantages, such as low cost, simplicity and availability for preparation at room temperature. In addition, binderless electrodes can be obtained by immersing the metal substrate in a suitable reaction solution, where the alloy electrode is directly anchored to the conductive substrate. Self-supported 3D durian-like $Bi_{0.75}Sb_{0.25}$ which exhibits a robust rate capability and cycling stability toward sodium storage, affording a reversible capability of 335 mAh·g^{-1} at a high rate of 2.5 A·g^{-1} have been designed and built through a template-free electrodeposition by Ni et al [33].

In this work, Bi-Sb alloy anodes for SIBs were successfully prepared by pulsed electrodeposition. The effects of deposition potential, deposition time and duty ratio on the negative electrode of Bi-Sb alloy were investigated systematically. The optimal anode material (marked by atomic ratio), which we believe is $Bi_{44.9}Sb_{55.1}$, can deliver a reversible discharge/charge capacities of 505 mAh·g^{-1}/496.7 mAh·g^{-1} at a high current density (1 A·g^{-1}), and still maintain a reversible discharge/charge capacities of 494.7 mAh·g^{-1}/481.9 mAh·g^{-1}, with a capacity retention rate of 97.9% after 50 cycles. As shown in **Table S1**, our work demonstrates superior capacity stability at high current density to other Bi-Sb anodes reported in previous literature for sodium-ion batteries [30-35].

2. Experiment details

2.1 Material synthesis

Firstly, linear sweep voltammetry (LSV) for the electrodeposition of Bi-Sb alloy was carried out on iviumstat potentiostat (IVIUM, Netherlands). Then, Bi-Sb alloy was synthesized by electrodeposition on copper substrate in acid Bi-Sb bath at room

temperature. The bath was comprised of $SbCl_3$, $C_4H_6O_6$, $C_6H_8O_7$, $BiCl_3$ and NaCl. Before each electrodeposition, 0.2 M HCl was used to scrub the oxide on the exterior of copper foil. A representative potential waveform of pulsed electrodeposition is presented in **Figure 1a**. The pulsed electrodeposition consisted of two steps: on and off steps. The bottom of **Figure 1a** indicates the cathodic and anodic currents passed during each step. The main purpose of the off step was to make deposition more uniform by removing surface protrusions. Therefore, a large change in the surface roughness was intentionally prevented by applying an off step every duty cycle [36]. The procedure for setting up a repeat in the system is as follows:

Step 1: -1.8 V for 2 s;

Step 2: 0.0 V for 1 s.

The Bi-Sb anode was prepared for 80 duty cycles (1 duty cycle = step 1 + step 2), the electrodes were cleaned with distilled H_2O and dried in a vacuum oven at 80 ℃ for 10 h. Subsequently, the integrated electrode was pressed to a disc with a diameter of 12 mm by using slicing machine, which was eventually utilized as the cathode. The sodium metal anode was purchased from China National Pharmaceutical Reagent Chemicals Co., Ltd. After removing oil from the paper, the oxidation layer on Na surface is removed, so the surface of the sodium block is covered in silver metal luster, and then is pressed into sodium foil, which is followed by being punched into a 12 mm circular sheet. The half-cell CR2025 was assembled in a glove box abounded by high purity argon (Vigor Technology (Suzhou) Co., Ltd.) at less than 0.02 ppm moisture, which uses Bi-Sb alloy as anode, a glass fiber separator (Whatman GF/D) as the separator and flat sodium metal as the cathode. The growth of Bi-Sb alloy on copper foil is shown in **Figure 1b**. Cu collector acted as working electrode and Pt plate acted as counter electrode in the bath with H_2O, $SbCl_3$, $C_4H_6O_6$, $C_6H_8O_7$, $BiCl_3$ and NaCl. The Bi-Sb alloy was directly deposited by pulsed electrodeposition on the copper foil [37]. **Figure 1c** is the internal structure of the battery. When it is on charge, sodium ions exit from the sodium metal into the electrolyte and pass through the gap on the separator to the Bi-Sb alloy. During discharge, ion transport is the opposite of the above process. Therefore, the electrode process of sodium ion battery is reversible [38].

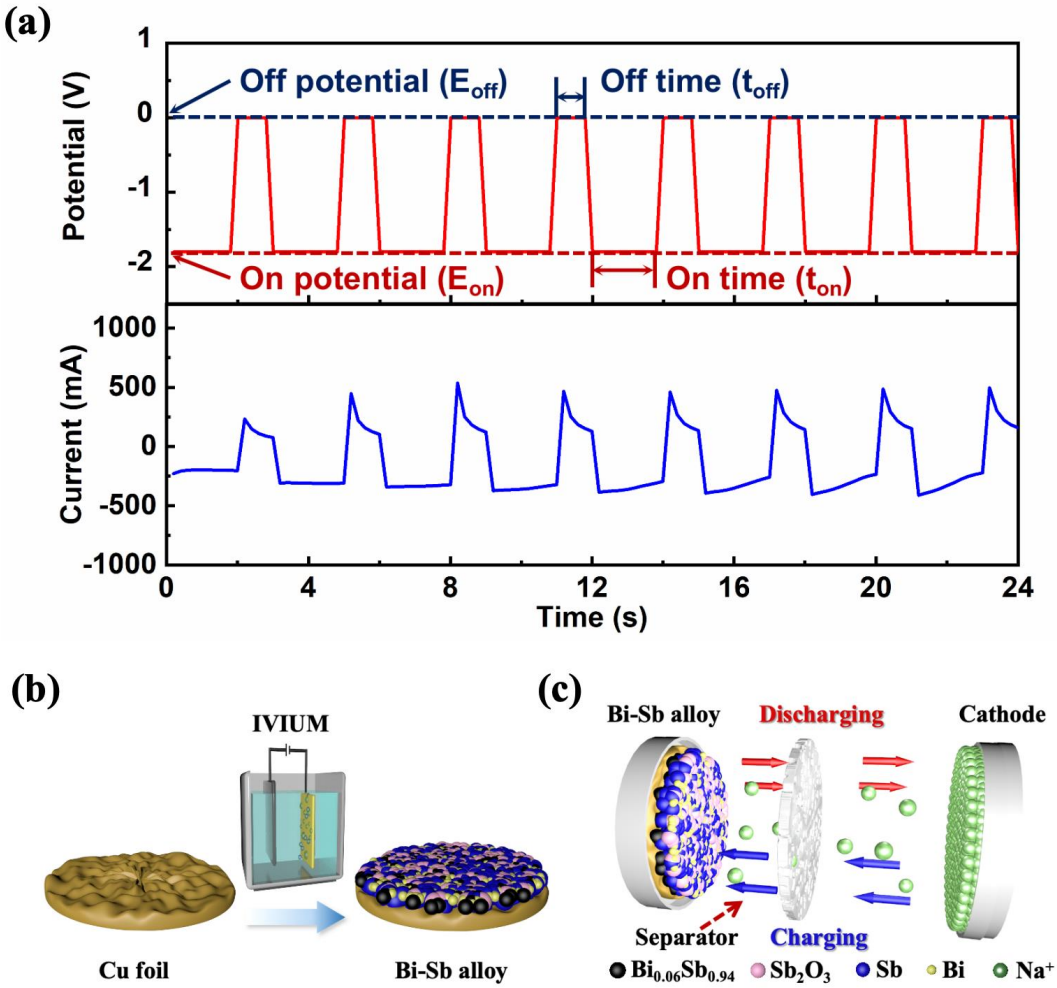

Figure 1 (a) A waveform of potential and the corresponding current response for pulsed electrodeposition with the definitions of off potential (E_{off}), off time (t_{off}), on potential (E_{on}), and on time (t_{on}), (b) Graphic illustration of electrodeposition process (Cu collector acted as working electrode and Pt plate acted as counter electrode in the bath with H_2O, $SbCl_3$, $C_4H_6O_6$, $C_6H_8O_7$, $BiCl_3$ and NaCl), (c) Internal structure of the cell.

2.2 Material characterization

The structural and morphological characteristics of $Bi_{44.9}Sb_{55.1}$, Bi and Sb samples were investigated by X-ray diffraction (XRD), scanning electron microscopy (SEM). XRD patterns were obtained by the XRD technique (Cu Ká, λ = 0.154 nm, 40 kV and 40 mA at a scanning rate of 5°/step from 20° to 80°). For in situ XRD, an electrolytic device consisted of the Bi-Sb alloy deposited on a carbon paper collector and an upper cover with a sealed Kapton film allowing penetration of the X-rays through and an electrode slice dipped in electrolyte, and the electrolyte ($NaClO_4$) filled the entire unit

as shown in **Figure S1**. The initial discharge/charge process was carried out at 1 $A \cdot g^{-1}$, and a spectrum was taken at an interval of 15 minutes. SEM images were measured on Hitachi S4800. X-ray Photoelectron Spectroscopy (XPS) measurements were performed with a Specs XR50 M monochromatic Al Kα source (1486.6 eV). The XPS survey and the detailed spectra were recorded with a constant analyzer pass energy of 20 eV. The composition of Bi-Sb alloy was reported for the sensitive determination of trace rhenium by inductively coupled plasma mass spectrometry (ICP-MS). Operando nuclear magnetic resonance experiments were performed on a home-made in-situ probe head and operando cell. All nuclear magnetic resonance experiments (NMR) were performed on a Bruker Avance III 400MHz spectrometer with a 2.5 mm probe head under spinning rates of 25kHz. The ^{23}Na single-pulse experiment was performed with a $\pi/4$ pulse length of 2.0 μs and a repetition time of 10 s.

2.3 Electrochemical measurements

The charge and discharge performance of the battery is carried out on NEWWARE battery circulator within the voltages (0.02 ~ 1.50 V vs. Na/Na^+) under constant current conditions. Cyclic Voltammetry (CV) curves were tested on ivium potentiostats at 0.25 $mV \cdot s^{-1}$ with a potential range of 0.02~1.50 V. Electrochemical impedance spectroscopy (EIS) measurements of $Bi_{44.9}Sb_{55.1}$ anode materials were accomplished at the same workstation with a frequency range of 10^5~0.1 Hz and 10 mV amplitude. After electrochemical cycling tests, the batteries were meticulously dismantled in the glove box. The cycled electrode ($Bi_{44.9}Sb_{55.1}$, pure Bi and pure Sb anodes) were cleaned with dimethyl carbonate (DMC) for several seconds and desiccated in air aimed at scanning electron microscopy imaging.

3. Results and discussion

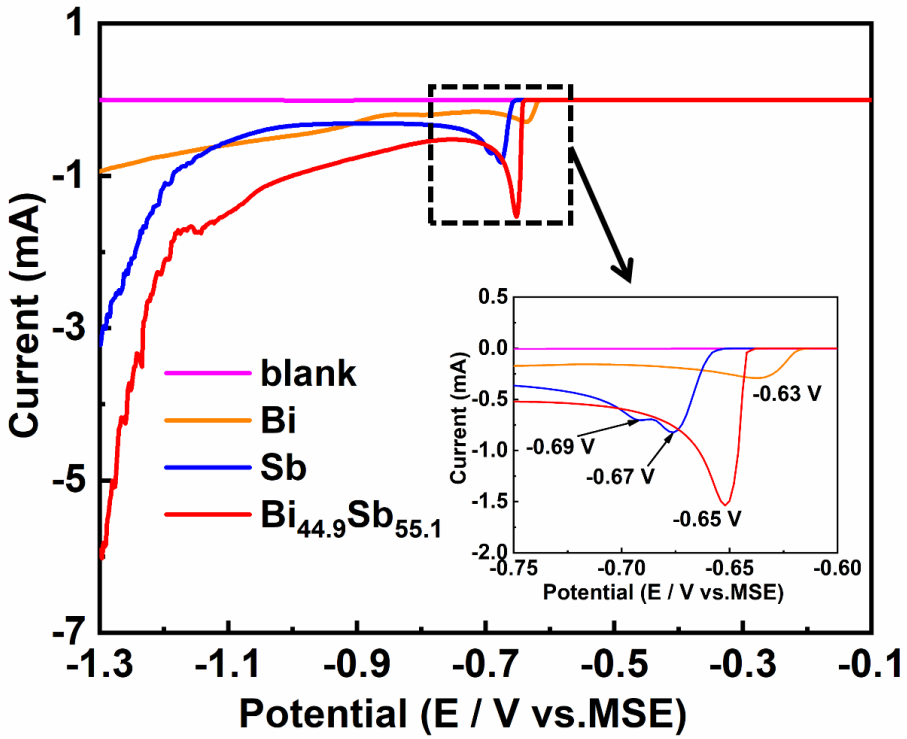

Figure 2 The current density-cathodic potential curves obtained by linear sweep voltammetry (LSV) in different plating solutions (Blank solution consists of $C_4H_6O_6$, $C_6H_8O_7$, and NaCl; Bi solution consists of $C_4H_6O_6$, $C_6H_8O_7$, $BiCl_3$ and NaCl; Sb solution consists of $C_4H_6O_6$, $C_6H_8O_7$, $SbCl_3$ and NaCl; $Bi_{44.9}Sb_{55.1}$ solution consists of $C_4H_6O_6$, $C_6H_8O_7$, $SbCl_3$, $BiCl_3$ and NaCl) at room temperature and partially enlarged images (insets).

Bi-Sb anode is marked by atomic ratio from ICP-MS as $Bi_{44.9}Sb_{55.1}$. **Figure 2** illustrates that linear sweep voltammetry (LSV) curves of the electrodeposition of $Bi_{44.9}Sb_{55.1}$. The current-potential curves of different electroplating solution were tested at 5 $mV \cdot s^{-1}$ with potentials ranging from 0.0 V to －1.5 V. No peak is found on the LSV curve of the solution in the absence of metal ions (**purple line**), indicating that no reaction occurs. When 0.038 M $BiCl_3$ was added into the blank solution, the measured LSV curve (**orange line**) shows a wide reduction peak at －0.63 V, indicating that Bi begins to deposit [39]. EDS test was carried out on the anode deposited in the plating solutions at －0.63 V. The presence of Bi can be visibly seen in **Figure S2a**, which proves that Bi is indeed deposited at －0.63 V. The element copper in Figure S1a is

from copper foil, and no other elements appear on the graph. When 0.079 M $SbCl_3$ was added into the blank electrolyte, the LSV curve (**blue line**) displays a reduction peak at a potential region from －0.67 V to －0.69 V, which are related to the adsorption of antimony-citrate complexes [40]. At －0.67 V, deposits are observed on the copper foil and a reduction peak is found, specifying that Sb begins to deposit [41]. EDS result in **Figure S2b** demonstrates the above phenomenon which clearly exhibits the characteristic peaks of element Sb. As the potential becomes negative, the current sharply increases, suggesting that the deposition quantity of Sb multiplies progressively, and oxygen evolution briskly increase shortly thereafter [42]. The orange and blue curves foresee the accumulation of metal ions, which can increase the rate of metal ion deposition. Then, when 0.079 M $SbCl_3$ and 0.038 M $BiCl_3$ were both added to the blank solution, the LSV curve (**red line**) shows a reduction peak at －0.65 V, which is between the deposition potential of Sb (－0.63 V) and Bi (－0.67 V). As the negative potential increases, the cathodic current increases sharply, indicating the co-deposition of Bi-Sb alloy and the occurrence of hydrogen evolution [43]. The EDS test was carried out on the alloy deposited in the electroplating solution at －0.65 V. The presence of Sb and Bi can be clearly seen in **Figure S2c**, which attests that Bi-Sb alloy is indeed deposited at －0.65 V. This indicates that high purity Bi-Sb alloys are

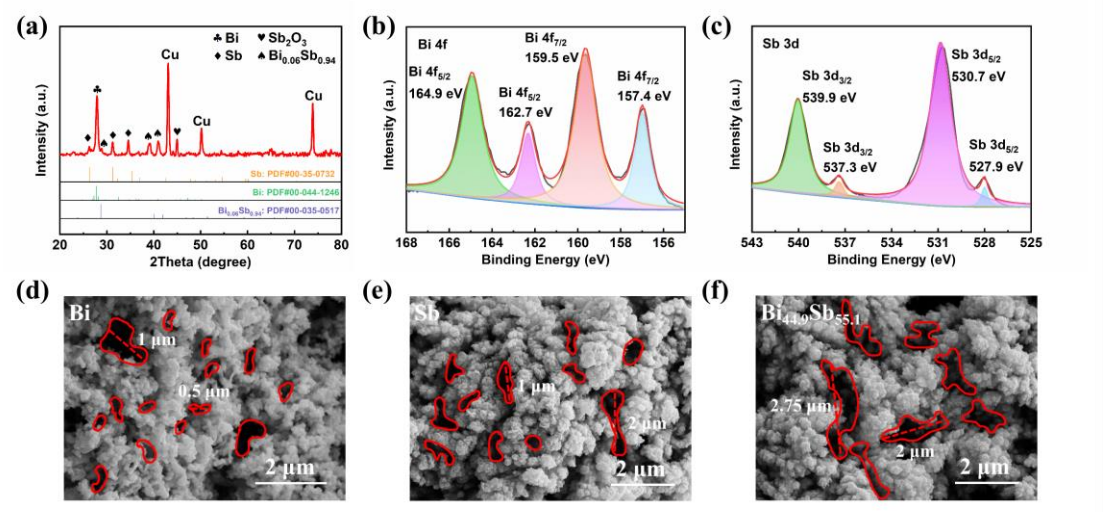

Figure 3 (a) XRD patterns of $Bi_{44.9}Sb_{55.1}$, pure Bi, pure Sb anodes prepared by pulsed electrodeposition; XPS spectra of (b) Bi 4f, (c) Sb 3d for $Bi_{44.9}Sb_{55.1}$ anode; High magnification SEM image and voids circled with the red contours of (d) pure Bi anode, (e) pure Sb anode, (f) $Bi_{44.9}Sb_{55.1}$ anode.

obtained by electrodeposition at this potential. With the addition of metal ions, the cathodic reduction potential gradually shifts negative, indicating that the addition of metal ions can increase the rate of metal ion deposition.

The crystallographic structures of $Bi_{44.9}Sb_{55.1}$, pure Bi and pure Sb anodes were analyzed using XRD (**Figure 3a** and **Figure S3**). The diffraction peaks of $Bi_{44.9}Sb_{55.1}$, pure Bi and pure Sb anodes are well indexed to Cu (JCPDS No.85-1326) at 43.3°, 50.4° and 74.1° corresponding to (111), (200) and (220) of the diffraction peaks of copper foil [44]. The XRD patterns of pure Bi at 27.1°, 37.9° and 39.6° match up with (012), (104) and (110) crystal planes of Bi (R-3m, JCPDS No.44-1246), respectively. The diffraction peak of Sb at 28.6° accords with the (012) of Sb (R-3m, JCPDS No.35-0732), the peaks located at 32.0°, 35.0° are the diffraction peaks of Sb_2O_3 (JCPDS No.05-0534) concurring with (400) and (331). The diffraction peaks of the $Bi_{44.9}Sb_{55.1}$ anode at 28.5°, 39.8° and 41.7° are referred to as (012), (104) and (110) of $Bi_{0.06}Sb_{0.94}$ (R-3m, JCPDS No.35-0517) [45]. The XRD results indicate that the prepared anode contains $Bi_{0.06}Sb_{0.94}$ and Sb_2O_3. XPS was utilized to analyze the elemental valence states of $Bi_{44.9}Sb_{55.1}$ anode materials. In the Bi 4f element spectrum (**Figure 3b**), the diffraction peaks of 162.7 eV and 157.4 eV fit in Bi $4f_{5/2}$ and Bi $4f_{7/2}$ of bismuth alloy, which tally with $Bi_{0.06}Sb_{0.94}$ in the results of XRD (**Figure 3a**). The peaks of 164.9 eV

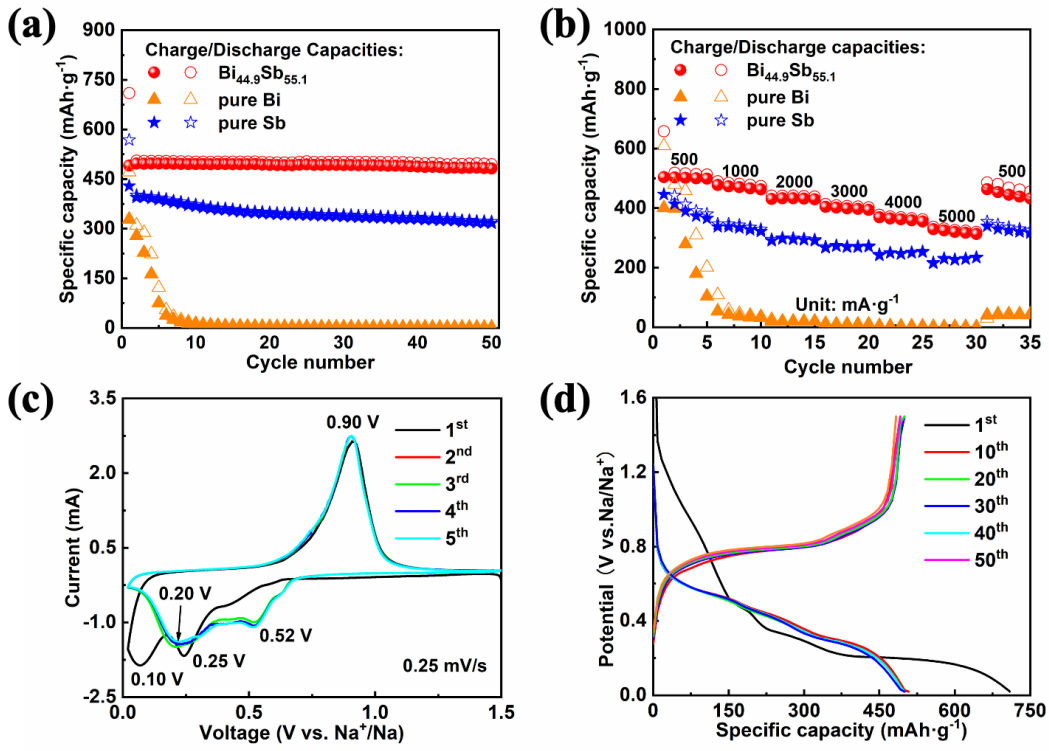

Figure 4 (a) Cyclic performance of $Bi_{44.9}Sb_{55.1}$, pure Bi and pure Sb anodes at 100 $mA \cdot g^{-1}$ in the first cycle, and at 1 $A \cdot g^{-1}$ from the second cycle with cut-off voltage of 0.02 to 1.50 V; (b) Rate performance of $Bi_{44.9}Sb_{55.1}$, pure Bi and pure Sb anodes at 0.02 V to 1.5 V; (c) First five CV curves of $Bi_{44.9}Sb_{55.1}$ anode with potential range from 0.02 V to 1.5 V (vs. Na/Na^+) in 0.25 $mV \cdot s^{-1}$; (d) Charge/Discharge profiles of $Bi_{44.9}Sb_{55.1}$ anode from different cycles.

and 159.5 eV belong to Bi $4f_{5/2}$ and Bi $4f_{7/2}$ respectively, which are related to Bi_2O_3 [27,31]. It is speculated that anodes may be exposed to air during the test since Bi has been partially oxidized into Bi_2O_3. In the element spectrum of Sb 3d (**Figure 3c**), the peaks at 539.9 eV and 537.3 eV belong to $3d_{3/2}$ of Sb, and the peaks of Sb $3d_{5/2}$ are 530.7 eV and 527.9 eV, among which 539.9 eV and 530.7 eV belong to Sb_2O_3. This is completely matched with the strong oxygen element in the full spectrum (**Figure S4**), and consistent with the XRD analysis results (**Figure 3a**) [44]. The peaks at 537.3 eV and 527.9 eV belong to Sb and Sb-based alloy which also tally with XRD results (**Figure 3a**) [46,47]. The Morphological characteristics of $Bi_{44.9}Sb_{55.1}$, pure Bi, and pure Sb anodes were characterized by SEM. The low magnification SEM images (**Figure S5b** and **c**) show that the pure Sb and $Bi_{44.9}Sb_{55.1}$ anodes have similar pine-like morphology. The mapping results indicate that Bi and Sb are evenly distributed. As shown in **Figure 3d** and **Figure 3e**, $Bi_{44.9}Sb_{55.1}$ and pure Sb anodes are composed of spherical particles consisting of acicular aggregates. Compared with the $Bi_{44.9}Sb_{55.1}$ anode, pure Bi anode has smaller voids and more dense aggregates. The size of these very small voids is about 0.5 μm. These extremely small voids are not conducive to electrolyte penetration, and these large aggregates and small voids are not conducive to reducing volume expansion during desodiation/sodiation. In comparison, the voids in the pure Sb anode are a little larger than that in the pure Bi anode, however, when compared with the voids of $Bi_{44.9}Sb_{55.1}$ anode, they are still too small, which is between 0.5 μm and 2 μm in size. Like pure Bi anode, these small voids are not suitable for the penetration of electrolytes and alleviate the volume effect during cycling. Nonetheless, the $Bi_{44.9}Sb_{55.1}$ anode has a satisfactory structure, and the appropriate voids (2 μm ~ 3 μm) are conducive to the penetration of electrolyte, which can cushion the volume expansion of the material during the charging/discharging process [44]. The **Figure S6a-c** shows EDS results of

pure Bi, pure Sb and $Bi_{44.9}Sb_{55.1}$ anodes, which indicate that pure Bi, pure Sb and $Bi_{44.9}Sb_{55.1}$ anodes are successfully prepared by pulsed electrodeposition [48].

To demonstrate the improved electrochemical performance of $Bi_{44.9}Sb_{55.1}$, the long-term cycling and rate performance were shown in **Figure 4a** and **Figure 4b** and compared with pure Bi and pure Sb anodes. During the first cycle, the current density is 100 $mA \cdot g^{-1}$, but it increases to 1 $A \cdot g^{-1}$ from the second cycle. As shown in **Figure S7a**, the initial coulombic efficiency of $Bi_{44.9}Sb_{55.1}$, pure Bi, and pure Sb anodes are 69.1%, 69.6%, and 65.6%, respectively. The low initial coulombic efficiency is attributed to SEI formation on the electrode surface and the irreversibility of the Sb_2O_3 conversion reaction [49]. Detailed comparison data is shown in **Table S2**, it can be seen that the initial discharge/charge specific capacities of pure Bi anode are 471.3 $mAh \cdot g^{-1}$/328.2 $mAh \cdot g^{-1}$ at 100 $mA \cdot g^{-1}$. The capacities drop rapidly after several cycles and hit a low of 0 $mAh \cdot g^{-1}$ at the 10^{th} cycle. Initial discharge/charge specific capacities of pure Sb anode (567.9/429.1 $mAh \cdot g^{-1}$) at 100 $mA \cdot g^{-1}$ are higher than that of pure Bi anode, but the specific capacity slowly declines (321.0 $mAh \cdot g^{-1}$/316.3 $mAh \cdot g^{-1}$) at 1 $A \cdot g^{-1}$ after 50 cycles, with the retention rate of only 80%. The speedy capacity dwindling is owing to the severe volume expansion caused by the insertion of large radius sodium ions [44]. In contrast, the $Bi_{44.9}Sb_{55.1}$ anode can deliver the discharge/charge capacities of 709.3 $mAh \cdot g^{-1}$/490.5 $mAh \cdot g^{-1}$ at 100 $mA \cdot g^{-1}$. From the second cycle, the discharge/charge capacities were 505.3 $mAh \cdot g^{-1}$/496.7 $mAh \cdot g^{-1}$ at 1 $A \cdot g^{-1}$, with a retention rate of 97.9% after cycling. The $Bi_{44.9}Sb_{55.1}$ anode has a unique microstructure and accumulation, hence its cycling stability is well-behaved and as a result the specific capacity is large [49,50]. Apparently, the $Bi_{44.9}Sb_{55.1}$ anode exhibits better electrochemical performance than pure Sb anode in the cycling performance due to the mechanical buffering provided by Bi in bi-active metal alloy mechanism [51]. **Figure S7b** depicts the influences of different substrates on the cycling performance of Bi-Sb anode under the same constant current condition (at 100 $mA \cdot g^{-1}$ in the first cycle and 1 $A \cdot g^{-1}$ from second cycle). Bi-Sb material deposited on copper foil with carbon coated on one side had an initial discharge/charge capacities of 543.4 $mAh \cdot g^{-1}$/425.9 $mAh \cdot g^{-1}$ at 100 $mA \cdot g^{-1}$, with a capacity retention rate of 88% after 50 cycles at 1 $A \cdot g^{-1}$. However, the Bi-Sb anode based on carbon paper has an initial discharge/charge capacities of 391.5 $mAh \cdot g^{-1}$/116.2 $mAh \cdot g^{-1}$ at 100 $mA \cdot g^{-1}$ and a capacity retention rate of 1.1% after 50 cycles. Moreover, The Bi-Sb based on steel wire has an initial discharge/charge capacity of

651.0 mAh·g^{-1}/565.9 mAh·g^{-1} at 100 mA·g^{-1} and a capacity retention rate of 1.2% after 50 cycles at 1 A·g^{-1}. The performance data of Bi-Sb anodes on different substrates are shown in the **Table S3**. It can be observed that the Bi-Sb anode based on copper foil has the greatest cycle performance among them.

Rate performance of $Bi_{44.9}Sb_{55.1}$, pure Bi and pure Sb anodes are shown in **Figure 4b**. Under the current density of 500, 1000, 2000, 3000, 4000 and 5000 mAh·g^{-1}, the specific charging capacities of $Bi_{44.9}Sb_{55.1}$ anode are 503.8 mAh·g^{-1}, 477.3 mAh·g^{-1}, 430.8 mAh·g^{-1}, 404.0 mAh·g^{-1}, 368.9 mAh·g^{-1} and 328.7 mAh·g^{-1} respectively. Pure Bi cannot return to the initial value after cycling under high current density, indicating that it has poor rate performance [52,53]. Meanwhile, pure Sb anode can resume its initial capacity even though it experiences capacity attenuation. The results show that the reversible capacity of the $Bi_{44.9}Sb_{55.1}$ anode can revert to the initial value as the current density going back to 500 mA·g^{-1}, which is predominantly attributed to the voids in the anode material. The voids are positive to the diffusion of the electrolyte and can effectively alleviate the volume expansion of the active metal during the cycle, so as to enhance its rate performance.

The electrochemical reaction kinetics of $Bi_{44.9}Sb_{55.1}$ anode were evaluated by adopting the method of cyclic voltammogram (CV). **Figure 4c** shows the CV curves of the $Bi_{44.9}Sb_{55.1}$ anode at 0.25 mV ·s^{-1} with voltage range from 0.02 V to －1.5 V during the first five cycles. In the first CV curve cycle, the reduction peak at 0.1 V is attributed to the SEI film formation, while the peak at 0.25 V is probably from the alloying process of Bi-Sb with Na [54]. Moreover, the oxidation peak at 0.9 V is caused by the desodiation process, which is from Na_3(Bi, Sb) to Na (Bi, Sb) and then to Bi-Sb alloy [55]. After the first cycle, the reduction peaks at 0.2 V and 0.52 V correspond to the formation of Na (Bi, Sb) and Na_3 (Bi, Sb) from a two-step alloying process, which stems from Bi-Sb alloy to Na (Bi, Sb) and then to Na_3 (Bi, Sb). The oxidation peak at 0.9 V can be well-overlapped, further demonstrating the high stability of $Bi_{44.9}Sb_{55.1}$ anode. In order to further investigate the alloying reaction, the charge/discharge curves of $Bi_{44.9}Sb_{55.1}$ anode were analyzed. **Figure 4d** displays charge/discharge curves of different cycles. In the first discharge curve, the potential plateau appears at 0.1 V, which is in accordance with the position of the reduction peak in the CV curve. The discharge curves of different cycles exhibit the plateaus at 0.2 V and 0.52 V correspond to the reactions from Bi-Sb alloy to Na (Bi, Sb) and then to Na_3(Bi, Sb). The charge curves at

0.9 V platform correspond to the reversible reaction of the anode, which are highly coherent with the CV curves [54,55]. **Figure S8a-c** displays the EIS and the equivalent circuit of the $Bi_{44.9}Sb_{55.1}$, pure Bi and pure Sb anodes before and after 50 cycles. The EIS spectra can be assigned to a semicircle of interface impedance in the high-frequency region, a semicircle of charge transfer impedance in the intermediate frequency region [56, 57]. After 50 cycles, the $Bi_{44.9}Sb_{55.1}$ anode displays the smallest semicircle, suggesting that a stable and thin SEI layer is formed. However, pure Bi and pure Sb anodes exhibit a much larger semicircle in comparison to the $Bi_{44.9}Sb_{55.1}$ anode. This indicates the severe pulverization of the pure Bi and pure Sb anodes would cause the overgrowth of the SEI layer and poor nanoparticles connection. The equivalent circuit diagram which contains the electrolyte resistance (R_s), SEI resistance (R_f), charge transfer resistance (R_{ct}) and the fitting data are as shown in **Table S4** [37]. The R_{ct} values of the $Bi_{44.9}Sb_{55.1}$ anode before and after 50 cycles demonstrates faster reaction kinetics with lower interface impedance and charge transfer impedance, which is closely related to the structural stability promoted by multiple dynamic supramolecular interactions [37,56]. The values of CPEs which can be observed in **Table S4** show a big change. As shown in the **Figure 3f** and **Figure 6c**, some subtle structural changes occurred on the surface of the electrode material during cycling, and these changes can expose more active sites and contribute to an increased capacitance as the value of CPE1 shown in **Table S4**. The reversible redox reactions at the anode surface can contribute to a higher capacitance after cycling. The formation of the SEI film during the cycle (shown in **Figure 6f**) prevents effective charge storage and can result in reduced capacitance which match the value of CPE2 shown in **Table S4** [56].

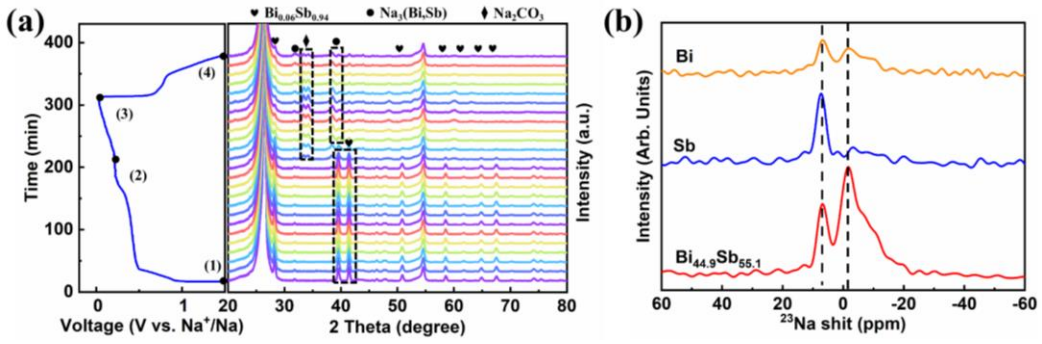

Figure 5 (a) Discharge/Charge curves of potential-time and in-situ XRD patterns of $Bi_{44.9}Sb_{55.1}$ anode with the current density of 1 $A \cdot g^{-1}$in the first cycle; (b) Single-pulse ^{23}Na NMR spectra of pure Bi, pure Sb and $Bi_{44.9}Sb_{55.1}$ anodes after the first discharge.

To gain a deeper understanding of the sodiation/desodiation mechanism of the $Bi_{44.9}Sb_{55.1}$ anode, in-situ XRD tests were performed during the first cycle, as depicted in **Figure 5a**. In the discharge process, diffraction peaks at 28.5°, 39.8°, 41.7°, 51.3°, 59°, 62.4°, 65.5°, and 68.0° belong to the $Bi_{0.06}Sb_{0.94}$. The diffraction peaks of the carbon paper appear at 25.8° and 54.3°, which do not change during the discharge/charging processes. This proves that the $Bi_{44.9}Sb_{55.1}$ anode does not react with the base. In the first stage of discharge from 1.5 V to 0.2 V, the diffraction peak of $Bi_{0.06}Sb_{0.94}$ begins to weaken and eventually disappear. In the second discharge stage from 0.2 V to 0.02 V, the diffraction peaks of Na_3(Bi, Sb) at 33.6°, 39.8° and 42.1° appear and increase, indicating that $Bi_{0.06}Sb_{0.94}$ phase is gradually turned into Na_3(Bi, Sb) [22,54]. The diffraction peaks appearing at 33.3°, 34.3° and 39.9° belong to Na_2CO_3, which is the main component of the SEI film [44]. In the subsequent charging process, the intensity of Na_3(Bi, Sb) peaks weaken continuously, and the diffraction peak of Na_2CO_3 does not disappear [37]. It is noteworthy that the diffraction peak of the final product Na_3(Bi, Sb) lies between the diffraction peaks of Na_3Bi and Na_3Sb, and the synchronous sodiation process of Bi and Sb can be attributed to the infinite miscibility and comparable physical-chemical properties between Bi and Sb [58].

To further confirm the composition of the SEI film of the pure Bi, pure Sb and $Bi_{44.9}Sb_{55.1}$ anodes when discharged to 0.02 V, the ^{23}Na NMR spectra were collected on the electrode surface (**Figure 5b**). The two peaks at 7.2 ppm and 0 ppm are respectively assigned to NaF and Na_2CO_3, both of which are the main constituents of the SEI film [59–64]. It should be noted that the peak intensity centered around 0 ppm on the $Bi_{44.9}Sb_{55.1}$ anode is the highest of the three electrodes. This suggests that the SEI film of the $Bi_{44.9}Sb_{55.1}$ electrode contains the greatest amount of Na_2CO_3. As a result, a thick and stable SEI film is formed, which is less susceptible to damage and results in an improved cycling stability of the electrode, which is consistent with the in-situ XRD results shown in **Figure 5a**.

To further explore the structural stability of $Bi_{44.9}Sb_{55.1}$, pure Bi and pure Sb anodes, the morphologies of the $Bi_{44.9}Sb_{55.1}$, pure Bi and pure Sb anodes were analyzed by SEM after cycling. **Figure 6a** reveals the SEM images of pure Bi anode after 50 cycles. It can be seen that Bi particles have been crushed. Compared with the images before cycle, the particles are loaded on the electrode surface after being crushed, and

the surface topography change to a large extent [18,21]. The EDS result (**Figure S9a**) proves that Bi, Cu, C, O and Na elements exist. The mapping diagram of pure Bi anode after 50 cycles (**Figure 6d**) exhibits that the spreading of Na, C, O, Bi and Cu elements in the selection are inconsistent. It can be inferred that SEI film was broken, and particles were disintegrated due to volume expansion. Surface topography leads to rapid decline in cycle performance. Although the mapping diagram of the Sb anode after cycling indicated the uniform distribution of Na, C, O, Sb, and Cu elements (**Figure 6e**), the SEM image (**Figure 6b**) revealed that the aggregate and void had increased in size. Because the surface topography of pure Sb anode is not seriously damaged and SEI film is not completely broken, the capacities do not decline rapidly. However, compared with the pure Sb anode surface before the cycle (**Figure S5**), the larger aggregate proves that the surface also experiences volume expansion, so the capacity decreases. Compared with the surface of pure Sb anode before cycles, the surface morphology changes only slightly, but it is not seriously damaged, there is a certain volume expansion, resulting in no rapid decline in capacity. This is consistent with the cycling performance and rate performance of pure Sb anode in **Figure 3a** and **Figure 3c**. Sb, Cu, C, O and Na can be precisely seen in the EDS diagram (**Figure S9b**). There is a compact SEI film on the surface of the $Bi_{44.9}Sb_{55.1}$ anode (**Figure 6c**), which can effectively prevent the microstructure failure of the anode and improve its structural stability, thus achieving better cycling performance, which is matched with the charge-discharge curves and CV curves in **Figure 3**. The results of EDS (**Figure S9c**) and mapping (**Figure 6f**) demonstrate that the $Bi_{44.9}Sb_{55.1}$ anode after 50 cycles has a uniform distribution of Bi, Sb, C, O and Na.

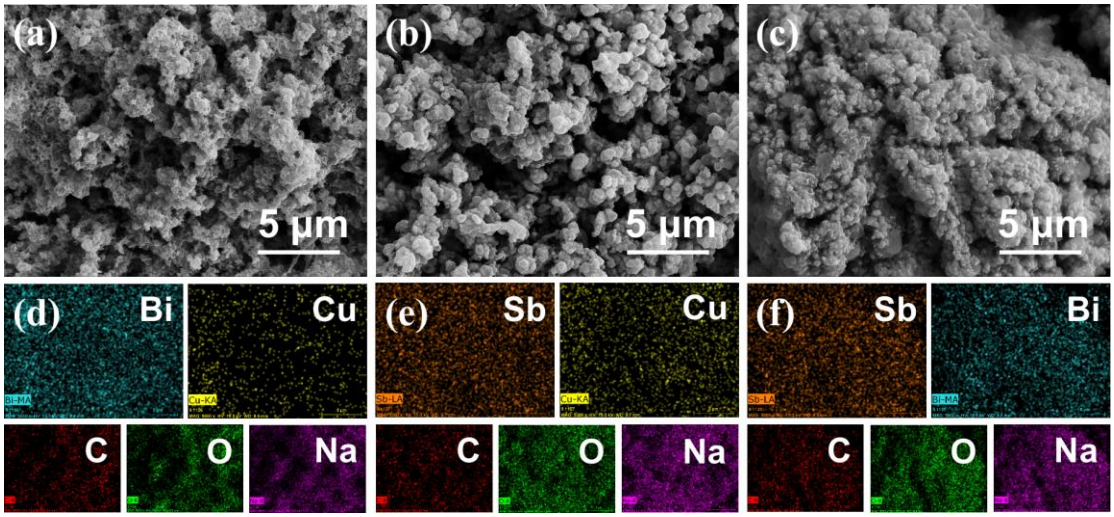

Figure 6 Low magnification SEM images of (a) pure Bi；(b) pure Sb；(c) $Bi_{44.9}Sb_{55.1}$ anodes and corresponding elemental mapping of (d) pure Bi；(e) pure Sb；(f) $Bi_{44.9}Sb_{55.1}$ anodes after 50 cycles.

4. Conclusions

In summary, we have successfully developed a novel pulsed electrodeposition technique that enables the synthesis of bi-active metal ($Bi_{44.9}Sb_{55.1}$) anodes for use in sodium ion batteries. This cost-effective and convenient method permits the preparation of alloy anodes with exceptional electrochemical properties at room temperature. The $Bi_{44.9}Sb_{55.1}$ anode delivers impressive reversible capacity and stable cycling performance even at high current densities. The remarkable cyclic stability and high specific capacity are attributed to the stable structure of the bi-active metal alloy, which offers adequate voids for efficient electron transport and ion diffusion, thereby mitigating volume expansion during cycling. Our findings offer valuable insights into the production of high-performance bi-active metal alloy anodes using pulsed electrodeposition techniques for sodium ion batteries operating under high current densities.

ACKNOWLEDGMENTS

This work was supported by the National Key R&D Program of China (No. 2019YFE0112000), the Fundamental Research Funds for the Provincial Universities of Zhejiang (Nos. 2021YW43 and 2021YW25), the Key R&D Program of Zhejiang Province of China (No. 2021C01190), and the Student Research Program of China Jiliang Univerisity (No. 2023X26090).

References:

1 A.G. Nguyen, H.T.T. Le, R. Verma, D.L. Vu, C.J. Park, Boosting sodium-ion battery performance using an antimony nanoparticle self-embedded in a 3D nitrogen-doped carbon framework anode, Chem. Eng. J. 2022; 429: 1323593. https://doi.org/10.1016/j.cej.2021.132359.

2 S. Sarkar, S. Roy, Y. Zhao, J. Zhang, Recent advances in semimetallic pnictogen (As, Sb, Bi) based anodes for sodium-ion batteries: Structural design, charge storage mechanisms, key challenges and perspectives, Nano Res. 2021; 14: 3690–3723. https://doi.org/10.1007/s12274-021-3334-y.

3 M.A. Ud Din, C. Li, L. Zhang, C. Han, B. Li, Recent progress and challenges on the bismuth-based anode for sodium-ion batteries and potassium-ion batteries, Mater. Today Phys. 2021; 21: 100486. https://doi.org/10.1016/j.mtphys.2021.100486.

4 Y. Li, F. Wu, Y. Li, M.Q. Liu, X. Feng, Y. Bai, C. Wu, Ether-based electrolytes for sodium ion batteries, Chem. Soc. Rev. 2022; 51: 4484–4536. https://doi.org/10.1039/D1CS00948F.

5 S. Liang, Y. Cheng, J. Zhu, Y. Xia, P.M. Buschbaum, A chronicle review of nonsilicon (Sn, Sb, Ge)-based lithium/sodium-ion battery alloying anodes, Small Methods. 2020; 4: 2000218. https://doi.org/10.1002/smtd.202000218.

6 I. Capone, J. Aspinall, H. J. Lee, A. W. Xiao, J. Ihli, M. Pasta, A red phosphorus-graphite anode for K-ion batteries. Mater. Today Energy. 2021; 21: 13633925. https://doi.org/10.26434/chemrxiv.13633925.v1.

7 S. Sarkar, S.C. Peter, An overview on Sb-based intermetallics and alloys for sodium-ion batteries: trends, challenges and future prospects from material synthesis to battery performance, J. Mater. Chem. A. 2021; 9: 5164–5196. https://doi.org/10.1039/D0TA12063D.

8 L. Guo, S. Vafakhah, M. Ding, M.E. Pam, Y. Wang, Y. Shang, S.Z. Huang, C.D. Gu, Y.V. Lim, H.Y. Yang, Direct antimony recovery from wastewater as anode materials for sodium-ion batteries, Mater. Today Energy. 2020; 16: 100403. https://doi.org/10.1016/j.mtener.2020.100403.

9 H. Fang, S. Gao, M. Ren, Y.H. Huang, F.Y. Cheng, J. Chen, F.J. Li, Dual-function presodiation with sodium diphenyl ketone towards ultra-stable hard carbon anodes for sodium-ion batteries, Angew. Chem. Int. Ed. 2023; 62: 202214717. https://doi.org/10.1002/anie.202214717.

10 L.N. Hu, X.Z. Li, Z.C. Lv, Y.R. Zhu, J.H. Zhang, T.F. Yi, Design of Sb_2Se_3-based nanocomposites for high-performance alkali metal ion batteries driven by a hybrid charge storage mechanism, Chem. Eng. J. 2022; 440: 135971. https://doi.org/10.1016/j.cej.2022.135971.

11 C. Delmas, Sodium and sodium-ion batteries: 50 years of research, Adv. Energy Mater. 2018; 8: 1703137. https://doi.org/10.1002/aenm.201703137.

12 Y. Kim, K.H. Ha, S.M. Oh, K.T. Lee, High-capacity anode materials for sodium-ion batteries, Chem. Eur. J. 2014; 20: 11980–11992. https://doi.org/10.1002/chem.201402511.

13 C. Wang, W. Tang, S. Jia, Y.C. Yan, D. Li, Y. Hu, J. Gao, H.L. Wu, M. Wang, S.H. Liu, H.H. Lai, T.T. Zou, L. Xu, J. Xiong, C. Fan, Benzene-bridged anthraquinones as a high-rate and long-lifespan organic cathode for advanced Na-ion batteries, Chem. Eng. J. 2021; 426: 131251. https://doi.org/10.1016/j.cej.2021.131251.

14 M.C. Liu, Z.Z. Yang, Y.F. Shen, S.H. Guo, J.Y. Zhang, X.P. Ai, H.X. Yang, J.F. Qian, Chemically presodiated Sb with a fluoride-rich interphase as a cycle-stable anode for high-energy sodium ion batteries, J. Mater. Chem. A. 2021; 9: 5639–5647. https://doi.org/10.1039/D0TA10880D.

15 B.H. Chen, L.Z. Yang, X.G. Bai, Q.Z. Wu, M. Liang, Y.X. Wang, N.Q. Zhao, C.S. Shi, B.Z. Zhou, C.N. He, Heterostructure engineering of core-shelled Sb@Sb_2O_3 encapsulated in 3D N-Doped carbon hollow-spheres for superior sodium/potassium storage, Small. 2021; 17: 2006824. https://doi.org/10.1002/smll.202006824.

16 T. Yang, J. Zhong, J. Liu, Y.J. Yuan, D.X. Yang, Q.A. Mao, X.Y. Li, Z.P. Guo, A general strategy for antimony-based alloy nanocomposite embedded in swiss-cheese-like nitrogen-doped porous carbon for energy storage, Adv. Funct. Mater. 2021; 31: 2009433. https://doi.org/10.1002/adfm.202009433.

17 G.M. Tomboc, Y. Wang, H. Wang, J. Li, K. Lee, Sn-based metal oxides and sulfides anode materials for Na ion battery, Energy Storage Mater. 2021; 39: 21–44. https://doi.org/10.1016/j.ensm.2021.04.009.

18 K.L. Luo, Z.Y. Leng, Z.D. Li, M.M. Ma, S. Li, W.P. Xie, D.Y. Wang, X.L. Cao, Z. Peng, Shielded electric field-boosted lithiophilic Sites: A Janus interface toward stable lithium metal anodes, Chem. Eng. J. 2021; 416: 129142. https://doi.org/10.1016/j.cej.2021.129142.

19 W.D. Pan, Y.F. Wang, X.L. Zhao, Y. Zhao, X.H. Liu, J. Xuan, H.Z. Wang, D.Y.C. Leung, High-performance aqueous Na-Zn hybrid ion battery boosted by "water-in-gel" electrolyte, Adv. Funct. Mater. 2021; 31: 2008783. https://doi.org/10.1002/adfm.202008783.

20 C. Huang, A.D. Xu, G.L. Li, H. Sun, S.P. Wu, Z.G. Xu, Y.R. Yan, Alloyed BiSb nanoparticles confined in tremella-like carbon microspheres for ultralong-life potassium ion batteries, Small, 2021; 17: 2100685. https://doi.org/10.1002/smll.202100685.

21 X.Y. Fan, Z. Jiang, L. Huang, X.X. Wang, J.X. Han, R.B. Sun, L. Gou, D.L. Li, Y.L. Ding, 3D porous self-standing Sb foam anode with a conformal indium layer for enhanced sodium storage, ACS Appl. Mater. Interfaces. 2020; 12: 20344–20353. https://doi.org/10.1021/acsami.9b23501.

22 J. Tian, H. Yang, C. Fu, M. Sun, L. Wang, T. Liu, In-situ synthesis of microspherical Sb@C composite anode with high tap density for lithium/sodium-ion batteries, Compos. Commun. 2020: 17: 177–181. https://doi.org/10.1016/j.coco.2019.12.005.

23 W.P. Kalisvaart, B.C. Olsen, E.J. Luber, J.M. Buriak, Sb-Si alloys and multilayers for sodium-ion battery anodes, ACS Appl. Energy Mater. 2019; 2: 2205–2213. https://doi.org/10.1021/acsaem.8b02231.

24 C.Y. Wu, W.T. Lian, L.J. Zhang, H.H. Ding, C.H. Jiang, Y.Y. Ma, W.H. Han, Y.M. Li, J.F. Zhu, T. Chen, C.F. Zhu, Water additive enhanced solution processing of alloy $Sb_2(S_{1-x}Se_x)_3$ -based solar cells, Sol. RRL. 2020; 4: 1900582. https://doi.org/10.1002/solr.201900582.

25 K.X. Yang, J.F. Tang, Y. Liu, M. Kong, B. Zhou, Y.C. Shang, W.H. Zhang, Controllable synthesis of peapod-like Sb@C and corn-like C@Sb nanotubes for sodium storage, ACS Nano. 2020; 14: 5728–5737. https://doi.org/10.1021/acsnano.0c00366.

26 H.M. Li, K.L. Wang, M. Zhou, W. Li, H.W. Tao, R.X Wang, S.J. Cheng, K. Jiang, Facile tailoring of multidimensional nanostructured Sb for sodium storage applications, ACS Nano.2019; 13: 9533–9540. https://doi.org/10.1021/acsnano.9b04520.

27 Z. Wang, J. Wang, J. Ni, L. Li, Structurally durable bimetallic alloy anodes enabled by compositional gradients, Adv. Sci. 2022; 9: 2201209. https://doi.org/10.1002/advs.202201209.

28 Y.Z. Liang, N. Song, Z.C.Y. Zhang, W.H. Chen, J.K. Feng, B.J. Xi, S.L. Xiong, Integrating Bi@C nanospheres in porous hard carbon frameworks for ultrafast sodium storage, Adv. Mater. 2022; 34: 2202673. https://doi.org/10.1002/adma.202202673.

29 A.N.Wang, W.W. Hong, L. Yang, Y. Tian, X.J. Qiu, G.Q. Zou, H.S. Hou, X.B. Ji, Bi-based electrode materials for alkali metal-ion batteries, Small. 2020; 16: 2004022. https://doi.org/10.1002/smll.202004022.

30 Z.Y. Wang, C.Q. Duan, D. Wang, K.Z. Dong, S.H. Luo, Y.G. Liu, Q. Wang, Y.H. Zhang, A.M. Hao, BiSb@Bi_2O_3/SbO_x encapsulated in porous carbon as anode materials for sodium/potassium-ion batteries with a high pseudocapacitive contribution, J. Colloid Interface Sci. 2020; 580: 429–438. https://doi.org/10.1016/j.jcis.2020.07.061.

31 W. Zhang, W. Yan, H.Q. Jiang, C. Wang, Y. Zhou, F.S. Ke, H.J. Cong, H.X. Deng, Uniform Bi-Sb alloy nanoparticles synthesized from MOFs by laser metallurgy for sodium-ion batteries, ACS Sustainable Chem. Eng. 2020; 8: 335–342, https://doi.org/10.1021/acssuschemeng.9b05474.

32 H. Gao, J. Niu, C. Zhang, Z. Peng, Z. Zhang, A dealloying synthetic strategy for nanoporous Bismuth-Antimony anodes for sodium ion batteries, ACS Nano.2018; 12: 3568–3577. https://doi.org/10.1021/acsnano.8b00643.

33 Ni, J., Li, X., Sun, M., Yuan, Y., Liu, T., Li, L., Lu, J. Durian-inspired design of Bismuth–antimony alloy arrays for robust sodium storage. ACS nano. 2020, 14(7): 9117-9124. https://doi.org/10.1021/acsnano.0c04366.

34 Usui H, Domi Y, Itoda Y, et al. Solid solution strengthening of bismuth antimonide as a sodium storage material. Energy & Fuels. 2021, 35(22): 18833-18838. https://doi.org/10.1021/acs.energyfuels.1c02987.

35 Zhao J, Xu J, Li Q, et al. BiSbx nanoalloys encapsulated by carbon fibers as high rate sodium ions storage anodes. Journal of Electroanalytical Chemistry. 2023, 939: 117452. https://doi.org/10.1016/j.jelechem.2023.117452.

36 Aryanfar A, Ghamlouche Y, Goddard III W A. Pulse Reverse Protocol for efficient suppression of dendritic micro-structures in rechargeable batteries. Electrochimica Acta. 2021, 367: 137469. https://doi.org/10.1016/j.electacta.2020.137469.

37 H.R. Shen, X.Y. Han, X.M. Zheng, B. Muniyandi, J.K. Wang, Q.L. Kang, M.G. Chen, Q. Wu, P.Y. Zhang, One-step electrochemical synthesis and optimization of Sb-Co-P alloy anode for sodium ion battery, Electrochimica Acta.2023; 438: 141529. https://doi.org/10.1016/j.electacta.2022.141529.

38 J. I. Kim, J. Heo, J. H. Park, Tailored metal oxide thin film on polyethylene separators for sodium-ion batteries, J. Electrochem. Soc. 2017; 164: A1965–A1969. https://doi.org/10.1149/2.1031709jes.

39 Y. Wu, Y. Gao, H. He, P. Zhang, Electrodeposition of self-supported Ni-Fe-Sn film on Ni foam: An efficient electrocatalyst for oxygen evolution reaction,

Electrochimica Acta. 2019; 301: 39–46. https://doi.org/10.1016/j.electacta.2019.01.151.

40 M. Tella, G.S. Pokrovski, Stability and structure of pentavalent antimony complexes with aqueous organic ligands, Chem. Geol.2012; 292–293: 57–68. https://doi.org/10.1016/j.chemgeo.2011.11.004.

41 D. Rajska, K. Motyka, M. Kozieł, D. Chlebda, A. Brzózka, G.D. Sulka, Influence of synthesis parameters on composition and morphology of electrodeposited Zn-Sb thin films, J. Ind. Eng. Chem. 2020; 84: 202–216. https://doi.org/10.1016/j.jiec.2019.12.035.

42 G.P. Kim, H.H. Sun, A. Manthiram, Design of a sectionalized MnO_2-Co_3O_4 electrode via selective electrodeposition of metal ions in hydrogel for enhanced electrocatalytic activity in metal-air batteries, Nano Energy. 2016; 30: 130–137. https://doi.org/10.1016/j.nanoen.2016.10.003.

43 J.J. Bu, J.J. Ru, Z.W. Wang, Y.X. Hua, C.Y. Xu, Y. Zhang, Y. Wang, Controllable preparation of antimony powders by electrodeposition in choline chloride-ethylene glycol, Adv. Powder Technol. 2019; 30: 2859–2867. https://doi.org/10.1016/j.apt.2019.06.027.

44 H.R. Shen, X.M. Zheng, Q.L. Kang, P. Dai, X.Y. Han, M.G. Chen, B. Muniyandi, Q. Wu, G.P. Tu, P.Y. Zhang, R. Huang, L. Deng, J.T. Li, L. Huang, S.G. Sun, High-performance and sodiation mechanism of a pulse potential-electrodeposited Sb-Zn alloy as an anode for sodium-ion batteries, Appl. Surf. Sci.2023; 609: 155243. https://doi.org/10.1016/j.apsusc.2022.155243.

45 H. Zhang, J.S. Son, J.Y. Jang, J.S. Lee, W.L. Ong, J.A. Malen, D.V. Talapin, $Bi_{1-x}Sb_x$ alloy nanocrystals: colloidal synthesis, charge transport, and thermoelectric properties, ACS Nano. 2013; 7: 10296–10306. https://doi.org/10.1021/nn404692s.

46 W.T. Jing, Y. Zhang, Y. Gu, Y.F. Zhu, C.C. Yang, Q. Jiang, N-Doped carbon nanonecklaces with encapsulated Sb as a sodium-ion battery anode, Matter. 2019; 1: 720–733. https://doi.org/10.1016/j.matt.2019.03.010.

47 I.M. Walton, J.M. Cox, C.A. Benson, D.G. Patel, Y.S. Chen, J.B. Benedict, The role of atropisomers on the photo-reactivity and fatigue of diarylethene-based metal-organic frameworks, New J. Chem. 2016; 40: 101–106. https://doi.org/10.1039/C5NJ01718A.

48 Y.F. Zhang, M. Li, F.B. Huang, Y.S. Li, Y.Q. Xu, F. Wang, Q.R. Yao, H.Y.

Zhou, J.Q. Deng, 3D porous Sb-Co nanocomposites as advanced anodes for sodium-ion batteries and potassium-ion batteries, Appl. Surf. Sci. 2020; 499: 143907. https://doi.org/10.1016/j.apsusc.2019.143907.

49 S. Kim, S. Qu, R. Zhang, P.V. Braun, High volumetric and gravimetric capacity electrodeposited mesostructured Sb_2O_3 sodium ion battery anodes, Small. 2019; 15: 1900258. https://doi.org/10.1002/smll.201900258.

50 S. Guo, H. Li, Y. Lu, Z. Liu, X. Hu, Lattice softening enables highly reversible sodium storage in anti-pulverization Bi-Sb alloy/carbon nanofibers, Energy Storage Mater. 2020; 27: 270–278. https://doi.org/10.1016/j.ensm.2020.02.003.

51 H. Gao, X.J. Yan, J.Z. Niu, Y. Zhang, M.J. Song, Y.J. Shi, W.S. Ma, J.Y. Qi, Z.H. Zhang, Scalable structural refining via altering working pressure and in-situ electrochemically-driven Cu-Sb alloying of magnetron sputtered Sb anode in sodium ion batteries, Chem. Eng. J. 2020; 388: 124299. https://doi.org/10.1016/j.cej.2020.124299.

52 Z. Lin, G. Wang, X. Xiong, J. Zheng, X. Ou, C. Yang, Ni-polymer gels-derived hollow NiSb alloy confined in 3D interconnected carbon as superior sodium-ion battery anode, Electrochimica Acta. 2018; 269: 225–231. https://doi.org/10.1016/j.electacta.2018.03.010.

53 M. Arnaiz, J.L. Gómez-Cámer, J. Ajuria, F. Bonilla, B. Acebedo, M. Jáuregui, E. Goikolea, M. Galceran, T. Rojo, High performance titanium antimonide $TiSb_2$ alloy for Na-ion batteries and capacitors, Chem. Mater. 2018; 30: 8155–8163. https://doi.org/10.1021/acs.chemmater.8b02639.

54 P. Xiong, J. Wu, M. Zhou, Y. Xu, Bismuth-antimony alloy nanoparticle@porous carbon nanosheet composite anode for high-performance potassium-ion batteries, ACS Nano. 2020; 14: 1018–1026. https://doi.org/10.1021/acsnano.9b08526.

55 M. Zhang, L. Ouyang, M. Zhu, F. Fang, J. Liu, Z. Liu, A phosphorus and carbon composite containing nanocrystalline Sb as a stable and high-capacity anode for sodium ion batteries, J. Mater. Chem. A. 2020; 8: 443–452. https://doi.org/10.1039/C9TA07508A.

56 Wan, X., Mu, T., Shen, B., Meng, Q., Lu, G., Lou, S., Yin, G. Stable silicon anodes realized by multifunctional dynamic cross-linking structure with self-healing chemistry and enhanced ionic conductivity for lithium-ion batteries. Nano Energy. 2022, 99: 107334. https://doi.org/10.1016/j.nanoen.2022.107334.

57 Ye, Q., Yuan, E., Shen, J., Ye, M., Xu, Q., Hu, X., Pang, H. Amphiphilic Polymer Capped Perovskite Compositing with Nano Zr-MOF for Nanozyme-Involved Biomimetic Cascade Catalysis. Advanced Science. 2023: 2304149. https://doi.org/10.1002/advs.202304149.

58 T.A. Hua, W. Wei, Q. Peng, X.Q. Ping, S. Qi, One-step synthesis of SnS_2 nanoflower/graphene nanocomposites with enhanced lithium ion storage performance, Acta Physico-Chimica Sinica. 2017; 33: 1621–1627. https://doi.org/10.3866/PKU.WHXB201704191.

59 K. Gotoh, ^{23}Na solid-state NMR analyses for Na-ion batteries and materials, batteries & supercaps. 2021; 4: 1267–1278. https://doi.org/10.1002/batt.202000295.

60 Y.X. Xiang, G.R. Zheng, Z.T. Liang, Y.T. Jin, X.S. Liu, S.J. Chen, K. Zhou, J.P. Zhu, M. Lin, H.J. He, J.J. Wan, S.S. Yu, G.M. Zhong, R.Q. Fu, Y.X. Li, Y. Yang, Visualizing the growth process of sodium microstructures in sodium batteries by in-situ ^{23}Na MRI and NMR spectroscopy, Nat. Nanotechnol. 2020; 15: 883–890. https://doi.org/10.1038/s41565-020-0749-7.

61 D.L. Smiley, D. Carlier, G.R. Goward, Combining density functional theory and ^{23}Na NMR to characterize Na_2FePO_4F as a potential sodium ion battery cathode, Solid State Nuclear Magnetic Resonance. 2019; 103: 1–8. https://doi.org/10.1016/j.ssnmr.2019.07.001.

62 R. Morita, K. Gotoh, K. Kubota, S. Komaba, K. Hashi, T. Shimizu, H. Ishida, Correlation of carbonization condition with metallic property of sodium clusters formed in hard carbon studied using ^{23}Na nuclear magnetic resonance, Carbon. 2019; 145: 712–715. https://doi.org/10.1016/j.carbon.2019.01.080.

63 R. Morita, K. Gotoh, M. Dahbi, K. Kubota, S. Komaba, K. Tokiwa, S. Arabnejad, K. Yamashita, K. Deguchi, S. Ohki, T. Shimizu, R. Laskowski, H. Ishida, States of thermochemically or electrochemically synthesized Na_xP_y compounds analyzed by solid state ^{23}Na and ^{31}P nuclear magnetic resonance with theoretical calculation, Journal of Power Sources. 2019; 413: 418–424. https://doi.org/10.1016/j.jpowsour.2018.12.070.

64 C. Ma, J. Alvarado, J. Xu, R.J. Clément, M. Kodur, W. Tong, C.P. Grey, Y.S. Meng, Exploring oxygen activity in the high energy P2-Type $Na_{0.78}Ni_{0.23}Mn_{0.69}O_2$ cathode material for Na-ion batteries, J. Am. Chem. Soc.

1 2017; 139: 4835–4845. https://doi.org/10.1021/jacs.7b00164.